Hindawi
Shock and Vibration
Volume 2017, Article ID 5716296, 14 pages
https://doi.org/10.1155/2017/5716296

Research Article

Enhanced Bearing Fault Detection Using Step-Varying Vibrational Resonance Based on Duffing Oscillator Nonlinear System

Yongbin Liu,[1,2] Zhijia Dai,[1] Siliang Lu,[1,2] Fang Liu,[1,2] Jiwen Zhao,[1,2] and Jiale Shen[1]

[1]*College of Electrical Engineering and Automation, Anhui University, Hefei, Anhui 230601, China*
[2]*National Engineering Laboratory of Energy-Saving Motor & Control Technology, Anhui University, Hefei, Anhui 230601, China*

Correspondence should be addressed to Siliang Lu; lusliang@mail.ustc.edu.cn

Received 28 November 2016; Revised 5 June 2017; Accepted 10 July 2017; Published 13 August 2017

Academic Editor: Mariano Artés

Bearing is a key part of rotary machines, and its working condition is critical in normal operation of rotary machines. Vibrational signals are usually analyzed to monitor the status of bearing. However, information on the status of bearing is always buried in heavy background noise; that is, status information of bearing is weaker than the background noise. Extracting the status features of bearing from signals buried in noise is difficult. Given this, a step-varying vibrational resonance (SVVR) method based on Duffing oscillator nonlinear system is proposed to enhance the weak status feature of bearing by tuning different parameters. Extraction ability of SVVR was verified by analyzing simulation signal and practical bearing signal. Experimental results show that SVVR is more effective in extracting weak characteristic information than other methods, including multiscale noise tuning stochastic resonance (SR), Woods–Saxon potential-based SR, and joint Woods–Saxon and Gaussian potential-based SR. Two evaluation indices are investigated to qualitatively and quantitatively assess the fault detection capability of the SVVR method. The results show that the SVVR can effectively identify the weak status information of bearing.

1. Introduction

Bearing plays an important role in ensuring the normal operation of mechanical components [1–3]. According to statistics, approximately 30% of rotary machine faults are caused by bearing failure. Vibrational signals acquired from bearing are usually used to monitor the working condition of bearings [4]. However, vibrational signals acquired by an accelerometer are always buried in heavy background noise. Weak signal detection (WSD) methods have been widely used to simultaneously enhance weak signals and suppress heavy noise. For example, Xiang and Shi proposed a WSD method based on information fusion and chaotic oscillator [5]. Moreover, Zhao et al. proposed a WSD method called improved harmonic product spectrum for train bearings fault detection [6]. Zhang et al. proposed a bearing fault detection method based on compressive measurements technology [7]. Additionally, Lu et al. proposed a new WSD method based on second-order stochastic resonance (SR) nonlinear physical model to enhance the periodicity of weak signals [8].

Two approaches in detection methods are available for denoising background noise. The first approach in WSD is noise suppression. The common related denoising methods include principal component analysis [9], kernel principal component analysis [10], empirical mode decomposition [11], independent component analysis [12], and wavelet transform [13].

The other approach in WSD involves the use of noise or high-frequency signal to enhance weak signals. The representative approaches include SR [14–16] and vibrational resonance (VR) [17]. The amplification mechanism of SR is described as follows: the energy of a particle in a bistable system is initially too small to allow the particle to move across the potential well. The energy of the particle becomes sufficiently high only with the help of a proper noise, which allows the particle to move across the well, resulting in interwell oscillation; this unconventional phenomenon is

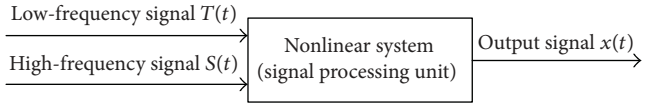

Figure 1: Simple block diagram of VR.

known as SR [18]. Since Benzi et al. proposed SR in 1981, SR has greatly attracted the attention of many researchers, especially those in the field of nonlinear system [19–21]. However, the use of SR is restricted by small parameters (driving frequency and amplitude of weak low-frequency signal are significantly smaller than one) [22].

Another nonnormal phenomenon named VR, a nonlinear filter similar to SR, was discovered by Landa and McClintock [23]. From the perspective of physics, a particle filled with energy is considerably weak and thus fails to move across a potential well. The particle can move across the potential well only with the assistance of the perturbation for an appropriate high-frequency signal. Owing to the perturbation of the high-frequency periodic force, the particle energy would be transferred, and the weak signal is instantaneously enhanced. VR was recently used as a special nonlinear filter in many nonlinear systems. For example, a time-delayed mechanism is used to control VR in a multistable system [24]; additionally, VR based on fractional-order damping in a Duffing system [25] and a new nonlinear physical model, namely, ultrasensitive vibrational resonance [26], were proposed to be applied in the field of nonlinear system.

A WSD method called step-varying vibrational resonance (SVVR) is proposed to extract the fault characteristic frequency of a series of defective bearing signals. In this paper, VR based on Duffing oscillator system combined with the parameter adjustment method is applied to solve the engineering problem. The optimal output signal can be obtained by selecting the optimal parameters. Finally, the periodicity of the weak signal would be improved.

This paper is organized as follows. Section 2 introduces a theoretical background of VR physical model. Section 3 combines the VR model with fourth-order Runge-Kutta (RK4) algorithm to obtain output signal. Section 4 uses a simulation signal to evaluate the filtering effect of SVVR method. Section 5 uses a set of defective bearing signals, which were processed by different WSD methods, to qualitatively and quantitatively verify the fault detection performance of SVVR. Section 6 provides a summary of this paper.

2. Theoretical Background of VR

2.1. VR Physical Model. Figure 1 shows the simple block diagram of VR. The diagram includes two signals with different frequencies, namely, weak low- and high-frequency periodic signals expressed as $T(t)$ and $S(t)$, respectively. The output signal $x(t)$ is obtained when two superimposed signals are processed by a nonlinear system. The VR model is expressed as follows:

$$\frac{d^2x}{dt^2} = -\frac{dV(x)}{dx} - \gamma\frac{dx}{dt} + T(t) + S(t), \tag{1}$$

where γ is the damping parameter, $T(t) = A\cos(2\pi ft)$, and $S(t) = B\cos(\Omega t)$, where f is driving frequency of $T(t)$ and Ω denotes angular frequency of $S(t)$. $V(x)$ is a bistable potential well function as shown in

$$V(x) = -\frac{1}{2}ax^2 + \frac{1}{4}bx^4, \tag{2}$$

where a and b denote the potential well parameters with positive values. Equation (3) is deduced by substituting $T(t)$, $S(t)$, and $V(x)$ into (1), as shown in

$$\frac{d^2x}{dt^2} = ax - bx^3 - \gamma\frac{dx}{dt} + A\cos(2\pi ft) + B\cos(\Omega t). \tag{3}$$

2.2. System Response Analysis. For brevity, let $dx/dt = y$; equation (3) can then be divided into the following equation sets:

$$\begin{aligned}\frac{dx}{dt} &= y\\ \frac{dy}{dt} &= ax - bx^3 - \gamma y + A\cos(2\pi ft) + B\cos(\Omega t).\end{aligned} \tag{4}$$

In (4), let $A = 0$, $B = 0$, $dx/dt = 0$, and $dy/dt = 0$; then three equilibria, namely, $X^*_+ = (x_+, y_+) = (\sqrt{a/b}, 0)$, $X^* = (x_0, y_0) = (0, 0)$, and $X^*_- = (x_-, y_-) = (-\sqrt{a/b}, 0)$, are obtained.

Given that (3) exists in two different frequencies, output $x(t)$ can be separated into fast and slow motions, respectively [27]. Let $x = X + \Psi$, where X and Ψ are slow and fast variables with periods of $T_L = 2\pi/2\pi f = 1/f$ and $T_H = 2\pi/\Omega$, respectively [25]. Equation (5) is deduced by substituting $x = X + \Psi$ into (3), as follows:

$$\begin{aligned}\frac{d^2X}{dt^2} + \frac{d^2\Psi}{dt^2} &= aX + a\Psi\\ &\quad - b\left(X^3 + 3X^2\Psi + 3X\Psi^2 + \Psi^3\right)\\ &\quad - \gamma\frac{dX}{dt} - \gamma\frac{d\Psi}{dt} + A\cos(2\pi ft)\\ &\quad + B\cos(\Omega t),\end{aligned} \tag{5}$$

and (6) is deduced from (5) as follows:

$$\begin{aligned}&\frac{d^2X}{dt^2} + \frac{d^2\Psi}{dt^2} + \gamma\frac{dX}{dt} + \gamma\frac{d\Psi}{dt} - aX - a\Psi + bX^3\\ &\quad + 3bX^2\Psi + 3bX\Psi^2 + b\Psi^3\\ &\quad = A\cos(2\pi ft) + B\cos(\Omega t),\end{aligned} \tag{6}$$

and the linear equation of the fast variable Ψ is shown in

$$\frac{d^2\Psi}{dt^2} + \gamma\frac{d\Psi}{dt} - a\Psi = B\cos(\Omega t), \tag{7}$$

and Ψ is obtained as shown in

$$\Psi = \frac{B}{\mu}\cos(\Omega t + \Theta), \tag{8}$$

in which

$$\mu^2 = \left(-a - \Omega^2\right)^2 + \left(\gamma\Omega\right)^2,$$
$$\Theta = -\tan^{-1}\frac{\gamma\Omega}{-a - \Omega^2}. \quad (9)$$

Equation (10) is obtained by substituting (8) into (6) and by integrating the total items at the range of $[0, T_H]$, as follows:

$$\frac{d^2X}{dt^2} + \gamma\frac{dX}{dt} + C_1X + bX^3 = A\cos\left(2\pi ft\right), \quad (10)$$

where $C_1 = 3bB^2/(2\mu^2) - a$.

The branch point is given by

$$F_c = \left[\frac{2\mu^2\left|a\right|}{3b}\right]^{1/2}. \quad (11)$$

The following equation is obtained considering the deviation Y of X from X^*:

$$\frac{d^2Y}{dt^2} + \gamma\frac{dY}{dt} + gY + 3bX^*Y^2 + bY^3 = A\cos\left(2\pi ft\right), \quad (12)$$

where $g = C_1 + 3bX^{*2}$. Equation (13) is obtained regardless of the nonlinear part in (12); that is, let $b = 0$; the deduced result is shown as follows:

$$\frac{d^2Y}{dt^2} + \gamma\frac{dY}{dt} + gY = A\cos\left(2\pi ft\right). \quad (13)$$

Equation (13) is obtained as $Y = A_L\cos(2\pi ft + \varphi)$, in which $A_L = A/\sqrt{S}$:

$$S = \left(g - \left(2\pi f\right)^2\right)^2 + \left(\gamma 2\pi f\right)^2,$$
$$\varphi = -\tan^{-1}\frac{\gamma 2\pi f}{g - \left(2\pi f\right)^2}. \quad (14)$$

Thus, the response amplitude Q is obtained as follows:

$$Q = \frac{1}{\sqrt{\left(g - \left(2\pi f\right)^2\right)^2 + \left(\gamma 2\pi f\right)^2}}. \quad (15)$$

Figure 2 shows the analysis result for resonance response. Parameters are configured as follows: $A = 0.1$, $f = 1/2\pi$, $\Omega = 10$, $a = 0.5$, $b = 1$, $\gamma = [0.05, 0.1, 0.15, 0.2]$, and B varies from 0 to 150 with 1 data interval. Response amplitude Q increases as B increases, subsequently peaks decrease, and finally Q gets close to zero. As shown in Figure 2, different values of γ induce the occurrence of the resonance phenomenon. Thus, optimal output signal is obtained by adjusting variables, such as γ, and other parameters.

3. SVVR Strategy

3.1. SVVR with Numerical Implementation. Section 2 provides the theoretical background of the VR model, which

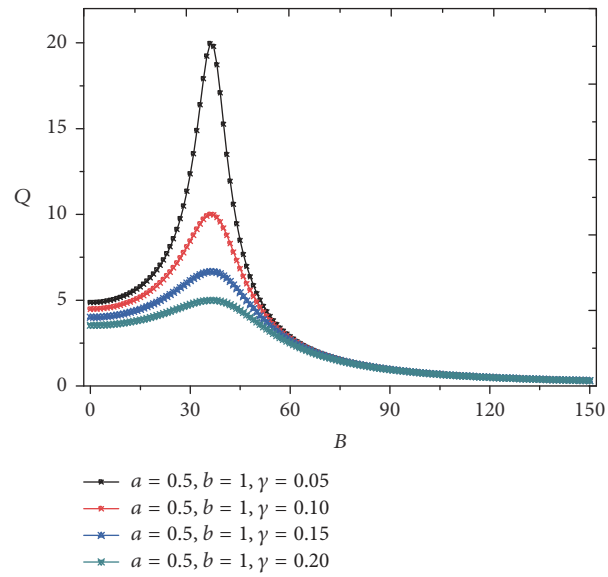

Figure 2: Resonance response curve.

is a continuous-time function. Given that practical bearing signals contain noise components, noise is added to the simulation signal. Equation (16) is then expressed as

$$\frac{d^2x}{dt^2} = -V'(x) - \gamma\frac{dx}{dt} + T(t) + S(t) + \xi(t), \quad (16)$$

where $\xi(t)$ is an additive Gaussian white noise with mean value $\langle\xi(t)\rangle = 0$ and autocorrelation coefficient $\langle\xi(t), \xi(0)\rangle = 2D\delta(t)$ [28, 29]. On the perspective of physics, white noise does not exist in nature. If the bandwidth of the added noise is far larger than the signal bandwidth, it can be approximately regarded as white noise. The noise intensity $2D = \sigma^2\Delta t$, where σ is an objective physical quantity which means the variance root of noise [30]. The sampling time-interval Δt is the noise correlation time.

The input signal consists of a weak low-frequency sinusoid $T(t)$, an additive Gaussian white noise $\xi(t)$, and an additional high-frequency sinusoid $S(t)$. The weak low-frequency sinusoid $T(t)$ is the driving signal.

The continuous-time function $x(t)$ of (16) is solved using

$$x_1 = -V'(x[n]) - \gamma y_1 + T[n] + S[n] + \xi[n];$$
$$x_2 = -V'\left(x[n] + \frac{y_1h}{2}\right) - \gamma y_2 + T[n] + S[n] + \xi[n];$$
$$x_3 = -V'\left(x[n] + \frac{y_2h}{2}\right) - \gamma y_3 + T[n+1] + S[n+1] + \xi[n+1]; \quad (17)$$
$$x_4 = -V'(x[n] + y_3h) - \gamma y_4 + T[n+1] + S[n+1] + \xi[n+1],$$

where

$$\begin{aligned}
y_1 &= y[n];\\
y_2 &= y[n] + \frac{x_1 h}{2};\\
y_3 &= y[n] + \frac{x_2 h}{2};\\
y_4 &= y[n] + x_3 h;\\
x[1] &= 0,\\
y[1] &= 0;\\
x[n] &= x[n-1] + \frac{(y_1 + 2y_2 + 2y_3 + y_4)h}{6},\\
&\qquad n = 2, 3, 4, \ldots, R;\\
y[n] &= y[n-1] + \frac{(x_1 + 2x_2 + 2x_3 + x_4)h}{6};\\
&\qquad n = 2, 3, 4, \ldots, R,
\end{aligned} \tag{18}$$

where discrete matrices $x[n]$, $y[n]$, $T[n]$, $S[n]$, and $\xi[n]$ are obtained by discretizing the continuous-time functions $x(t)$, $y(t)$, $T(t)$, $S(t)$, and $\xi(t)$, respectively. Discrete output $x[n]$ is obtained through multiple iterative computation. Signal-to-noise ratio (SNR) is selected as an evaluation index. The definition of SNR is shown as follows:

$$\begin{aligned}
\mathrm{SNR} &= 10\log_{10}\frac{P_s}{\sum_{i=1}^{M/2} P_i - P_s}\\
&= 10\log_{10}\frac{P\left[\mathrm{round}\left(f_d/\Delta f\right)+1\right]}{\sum_{i=1}^{M/2} P[i] - P\left[\mathrm{round}\left(f_d/\Delta f\right)+1\right]},
\end{aligned} \tag{19}$$

where M is the discrete-time array length, $P[\cdot]$ denotes the signal's power in spectrum, P_s denotes the driving signal's energy, P_i is the input signal's total energy, the sum term $\sum_{i=1}^{M/2} P_i - P_s$ denotes the energy of the noise components, and f_d is the driving frequency. Frequency resolution is defined as $\Delta f = f_s/M$, where f_s is the sampling frequency of input signal.

3.2. Algorithm Flow Chart of SVVR Method. Six parameters, namely, bistable potential well parameters a and b, damping parameter γ, amplitude of high-frequency signal B, angular frequency of high-frequency signal Ω, and calculation step of RK4 algorithm h, can be tuned. The optimal output signal can be obtained when each adjustable parameter searches for an optimal value. Figure 3 shows the algorithm flow chart, and the algorithm steps are demonstrated as follows.

(1) Signal Preprocessing. The uncorrelated noise signals possibly affect the accuracy of fault signal detection. A band-pass filter is used to eliminate the uncorrelated noise components in the first step. Subsequently, Hilbert transform is used to demodulate the fault signal, which was processed by the band-pass filter.

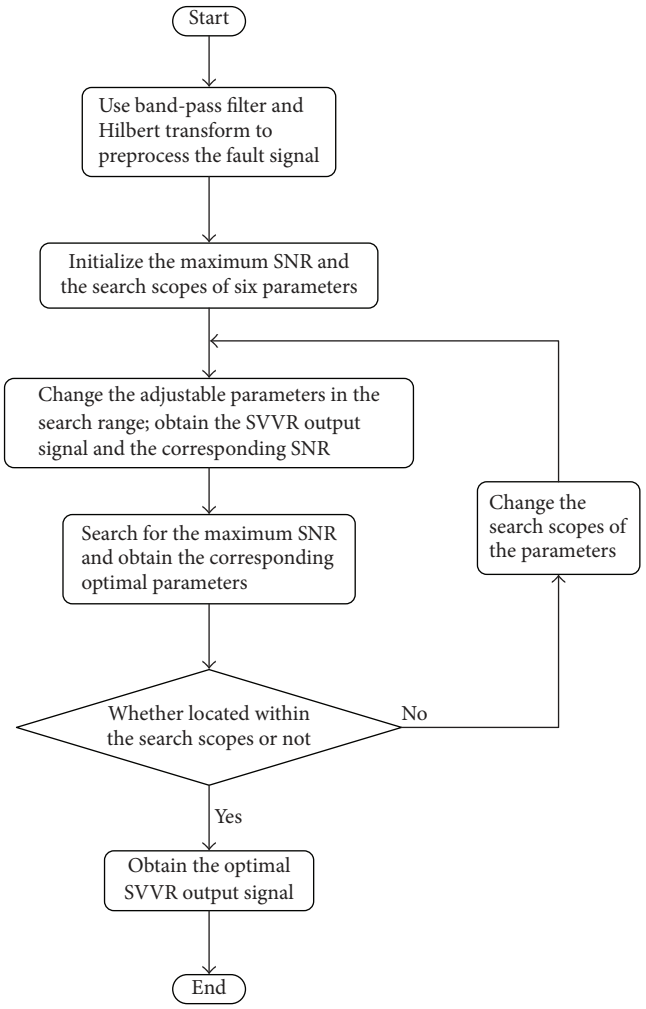

Figure 3: The algorithm flow chart.

(2) Parameter Initialization. First, an initialized value for maximum SNR is given. The search scopes of the adjustable parameters are subsequently initialized. A six-layer loop is used to delimit the search scopes.

(3) Determination of the Optimal Parameters and Maximum SNR. The output signal is obtained using (17). Each tuned variable then obtains an independent numerical value. The objective function is shown in (20). When the optimal parameters a_{opt}, b_{opt}, γ_{opt}, B_{opt}, Ω_{opt}, and h_{opt}all lay within the search scopes, the fourth step is performed; otherwise, the process returns to the second step. Five tuned parameters, namely, a, b, B, Ω, and h, should fall within the bounded ranges even if their theoretical values range from 0 to +inf.

$$\begin{aligned}
&\text{maximize} \quad \mathrm{SNR}\left(a, b, \gamma, B, \Omega, h\right)\\
&\text{subject to} \quad a, b, B, \Omega, h \in (0, +\infty),\\
&\qquad\qquad\quad \gamma \in (0, 1).
\end{aligned} \tag{20}$$

(4) Signal Postprocessing. When the optimal ranges of parameters are determined, the maximum SNR and optimal

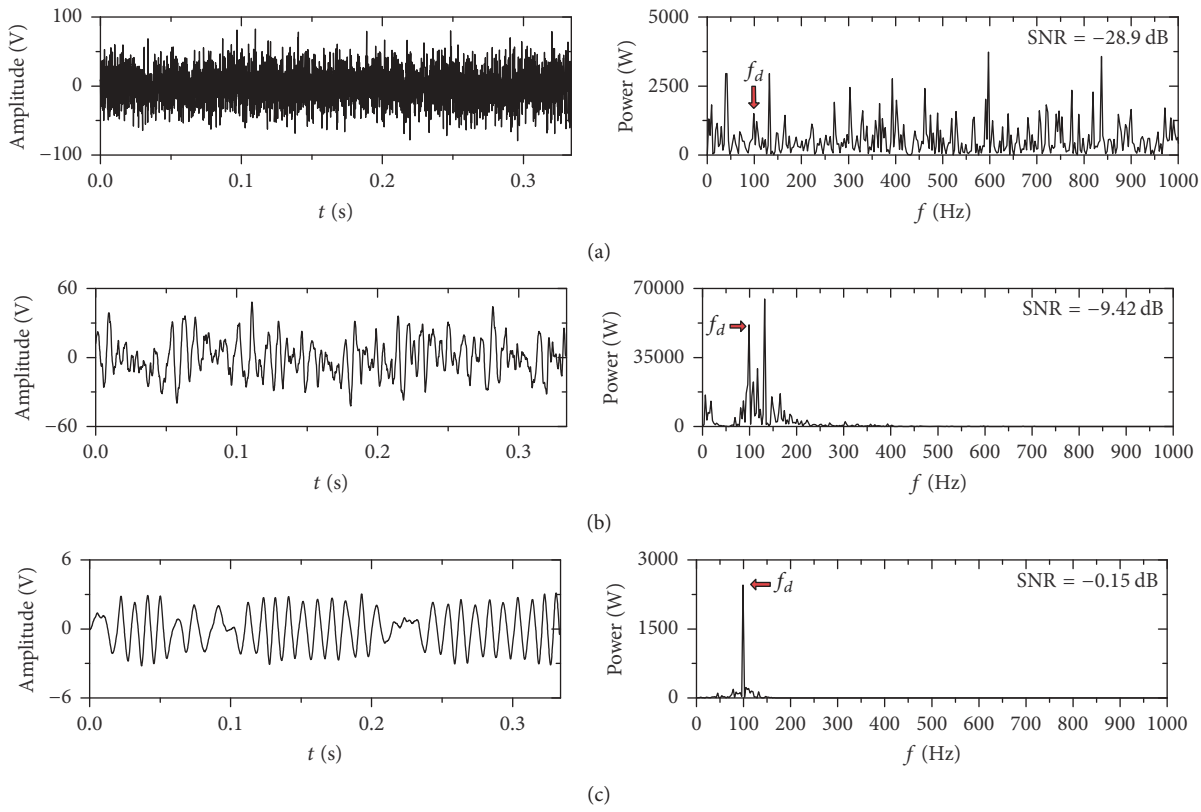

Figure 4: Comparison of the periodicity and noise suppression performance of two WSD methods: (a) input signal; (b) MSTSR output signal (optimal parameters: $a = 0.7$, $b = 8e-4$, $h = 0.01$, and $K = 6$); and (c) optimal SVVR output signal (optimal parameters: $a = 1.9$, $b = 2.9$, $\gamma = 0.009$, $h = 0.015$, $B = 1.6$, and $\Omega = 23236$ rad/s).

parameter values are acquired simultaneously. Finally, the optimal output signal is obtained according to the optimal parameters.

4. The Performance Evaluation of SVVR

4.1. Simulation Signal Analysis. A simulation signal is used to verify the validity of the SVVR method. Multiscale noise tuning SR (MSTSR) is implemented in the simulation signal to highlight the superiority of the SVVR method [13]. MSTSR is a parameter-tuning approach, and four parameters, namely, wavelet decomposition level K, bistable potential well parameters a and b, and calculation step h, can be tuned. The difference between MSTSR and traditional SR methods depends on noise types. The noise in the traditional SR is an additive Gaussian white noise, whereas that in MSTSR is a multiscale noise. Thus, the filtering effect of MSTSR method is more effective than that of the conventional SR method. A key step in MSTSR lies in the construction of the $1/f$ noise. Discrete wavelet transform is applied to obtain the multiscale noise and reconstruct the input signal. RK4 algorithm is then conducted to solve the equation set. Finally, MSTSR output can be obtained.

A simulation signal is constructed by combining a sinusoid with an additive Gaussian white noise. The number of sampling points R is 4000, and the sampling frequency f_s is 12 kHz. The parameters of the input signal are set as follows: $A = 1$, $f_d = 100$ Hz, and $D = 25$. Processed results are shown in Figure 4. Figure 4(a) shows the raw signal both in time and in frequency domains. Noise components are considerably heavy such that the wave interval is buried in heavy background noise. From the perspective of power spectrum, noise interference is obvious and the driving frequency f_d cannot be efficiently recognized in the frequency domain. Figure 4(b) displays the processed MSTSR output signal. The periodicity of MSTSR signal is better than that of the original signal, and its waveform interval is distributed optionally. Although f_d can be pinpointed in the power spectrum, the energy of one noise component is higher than f_d. Figure 4(c) displays the processed optimal SVVR output signal. Its periodicity improved compared with that of the MSTSR output signal, and f_d is extracted in the frequency domain and most of the noise components are suppressed at the same time. The SNRs from each subfigure imply that the SVVR method is more effective in extracting the weak feature component than the MSTSR method. A higher SNR indicates a more accurate detection performance for fault signals [31–34].

4.2. Frequency Response Analysis. The analysis result of frequency response is shown in Figure 5. The parameters are configured as follows: $a = 0.0008$, $b = 1000$, $B = 0.8$, $\Omega = 8971$ rad/s, $h = 0.062$, $\gamma = 0.3$, $A = 1$, $D = 2$,

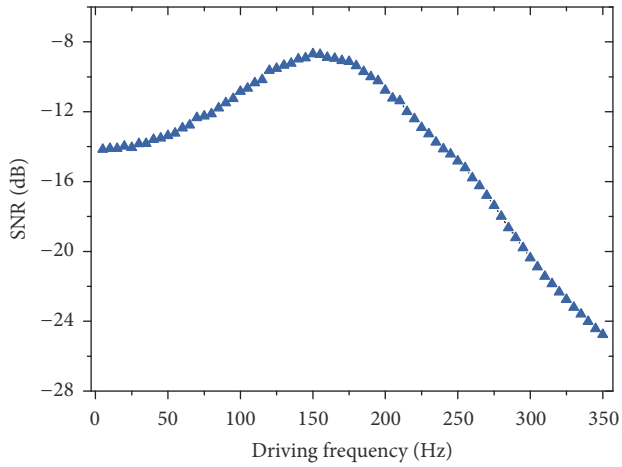

Figure 5: Frequency response analysis for SVVR.

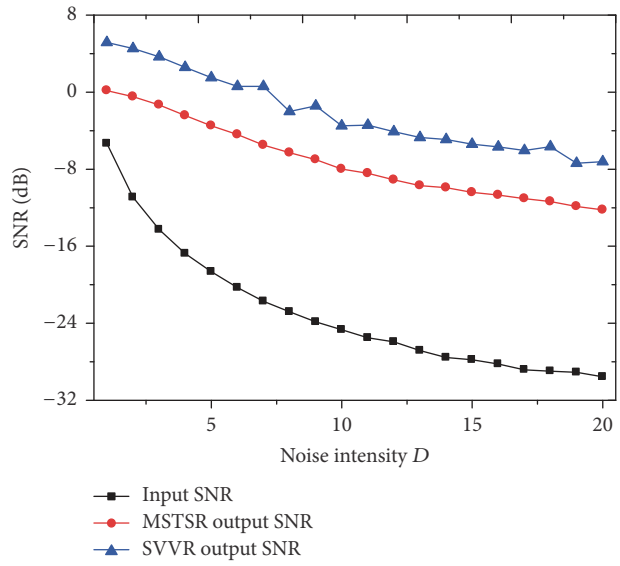

Figure 6: Performance analysis of noise suppression using different WSD methods.

f_s = 3 kHz, R = 3000, and f_d is changed from 5 Hz to 350 Hz with 5 Hz data interval. Each data point is processed approximately 1000 times using the ensemble average method to display the smooth performance of the curve. The frequency response analysis of SVVR shows that it is a band-pass filter. Consequently, SVVR can filter both high- and low-frequency noise components.

4.3. Antinoise Performance Analysis. The analysis result of antinoise performance is displayed in Figure 6. The parameters are configured as follows: f_d = 100 Hz, A = 1, and D is changed from 1 to 20 with one-step variation. Figure 6 shows that all the SNRs decrease with the increase in D. Although Figure 6 presents a decaying trend, the SVVR output SNR is higher than the MSTSR output SNR and input SNR. Thus, SVVR shows a better antinoise capability compared with MSTSR.

Table 1: Physical dimensions of the tested rolling bearing.

Roller diameter (inch; d_1)	Pitch diameter (inch; d_2)	Number of the rollers (r)
0.3126	1.537	9

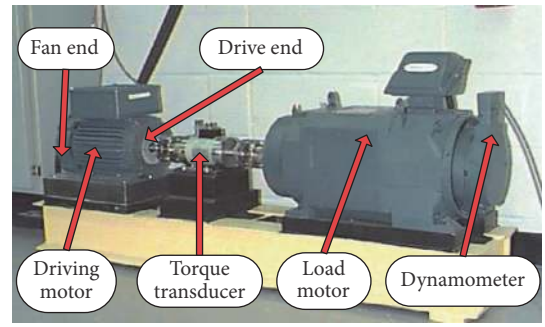

Figure 7: Experimental test platform.

5. Engineering Application

In this section, the defective bearing signals are selected for analysis. Two WSD methods, namely, the Woods–Saxon potential-based SR (WSSR) [35] and the joint Woods–Saxon and Gaussian potential-based SR (WSGSR) [36], are applied to evaluate the fault extraction capability of SVVR. The mathematical expression of the Woods–Saxon potential is shown in

$$U_{\mathrm{ws}}(x) = -\frac{V_0}{1+\exp\left(\left(|x|-R_1\right)/c\right)}, \tag{21}$$

where V_0, R_1, and c are the depth, radius, and the steep extent of the Woods–Saxon potential, respectively. The expression of the Gaussian potential is

$$U_{\mathrm{G}}(x) = -V_1 \exp\left(-\frac{x^2}{{R_2}^2}\right), \tag{22}$$

where V_1 and R_2 are the depth and radius of the Gaussian potential, respectively. By combining (21) and (22), then the Woods–Saxon and Gaussian joint potential is deduced in

$$\begin{aligned} U_{\mathrm{wsG}}(x) &= U_{\mathrm{ws}}(x) - U_{\mathrm{G}}(x) \\ &= -\frac{V_0}{1+\exp\left(\left(|x|-R_1\right)/c\right)} \\ &\quad + V_1 \exp\left(-\frac{x^2}{{R_2}^2}\right). \end{aligned} \tag{23}$$

The acquired defective bearing signals are downloaded freely from the bearing data center of Case Western Reserve University (CWRU) [37]. The experimental test platform and physical dimension of the tested bearing are shown in Figure 7 and Table 1, respectively. The sampling frequency f_s is 12 kHz, and the number of sampling points R is 8192. The fault characteristic frequencies for the inner race, outer race, and rolling element are denoted as f_{BPFI}, f_{BPFO}, and f_{BSF},

Table 2: Acquisition information of the rolling bearing from the bearing data center of CWRU.

Fault types	Size of fault ($D \times W$; inch)	Approximate rotational speed (r/min)	Theoretical fault characteristic frequency (Hz)
Inner race	0.011×0.014	1797	162.2
Outer race	0.011×0.021	1730	103.4
Rolling element	0.011×0.014	1772	139.2

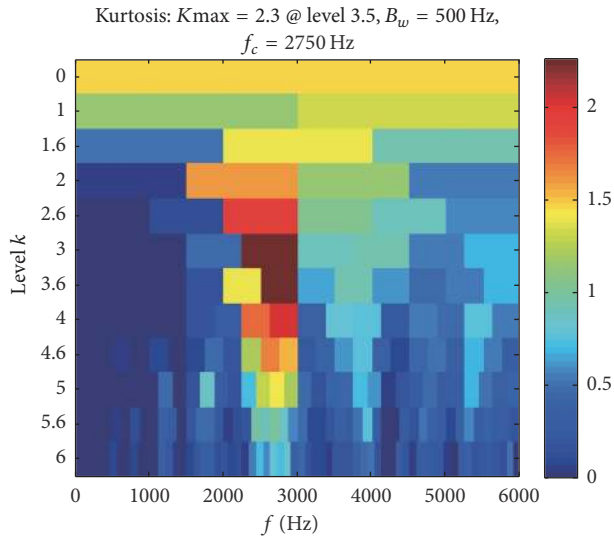

Figure 8: Processed results using fast kurtogram for detecting an inner race fault. Central frequency f_c = 2750 Hz, bandwidth B_w = 500 Hz, and level k = 3.5.

respectively. These fault characteristic frequencies can be calculated according to the physical dimension of the tested bearing [38]. The related calculation equations for different fault characteristic frequencies are shown as follows:

$$f_{\mathrm{BPFI}} = \frac{rf_r}{2}\left(1 + \frac{d_1}{d_2}\cos\alpha\right),$$
$$f_{\mathrm{BPFO}} = \frac{rf_r}{2}\left(1 - \frac{d_1}{d_2}\cos\alpha\right), \quad (24)$$
$$f_{\mathrm{BSF}} = \frac{f_r d_2}{2d_1}\left[1 - \left(\frac{d_1}{d_2}\cos\alpha\right)^2\right],$$

where r is the quantity of the rollers, d_1 is the roller diameter of the bearing, d_2 is the pitch diameter of the bearing, α is the bearing's contact angle, and f_r is the rotating frequency of the bearing, respectively. The rolling bearing size and the fault characteristic frequencies at different locations of the fault bearing are listed in Table 2.

5.1. Fault Detection for the Inner Race of the Bearing. The bearing signal with defective inner race is initially selected for analysis. Acquired vibrational signals in the time and frequency domains are shown in Figure 9(a). The impulse interval in the time domain is difficult to recognize because of the considerably poor periodicity. Then, a band-pass filter is used to filter the uncorrelated noises of the original fault signal. Recently, many new methods have been proposed to determine the bandwidth and central frequency of the band-pass filter [39–42]. The fast kurtogram method is introduced in this section to choose the proper bandwidth and central frequency of the band-pass filter automatically and intelligently. The fast kurtogram is used to detect the inner race, outer race, and rolling element of the defective bearings, and the processed results are shown in Figures 8, 10, and 12, respectively.

Then, Hilbert transform is used to demodulate the fault signal which was processed by the band-pass filter. The processed results of the enveloped signal are displayed in Figure 9(b). It can be seen from Figure 9(b) that the fault characteristic frequency f_{BPFI} can be pointed out from the frequency domain, but the noise interference is significantly heavy, such that f_{BPFI} is overwhelmed by the noise components. Therefore, MSTSR is used to enhance the weak signal. The analyzed results are displayed in Figure 9(c). The time domain shows that the periodicity has been improved, but the impulse interval is still disturbed by the noise. From the view of the frequency domain, some low-frequency components are higher than f_{BPFI}. The processed results for WSSR and WSGSR output signals are shown in Figures 9(d) and 9(e), respectively. Although the periodicities of the MSTSR, WSSR, and WSGSR output signals are better than the envelope signal, the noise components are higher than f_{BPFI} in their corresponding frequency domains. The processed results of the SVVR output signal are shown in Figure 9(f). The periodicity in the time domain is better than those of the other signals, and the impulse interval is recognized. The power of f_{BPFI} is the highest one in the power

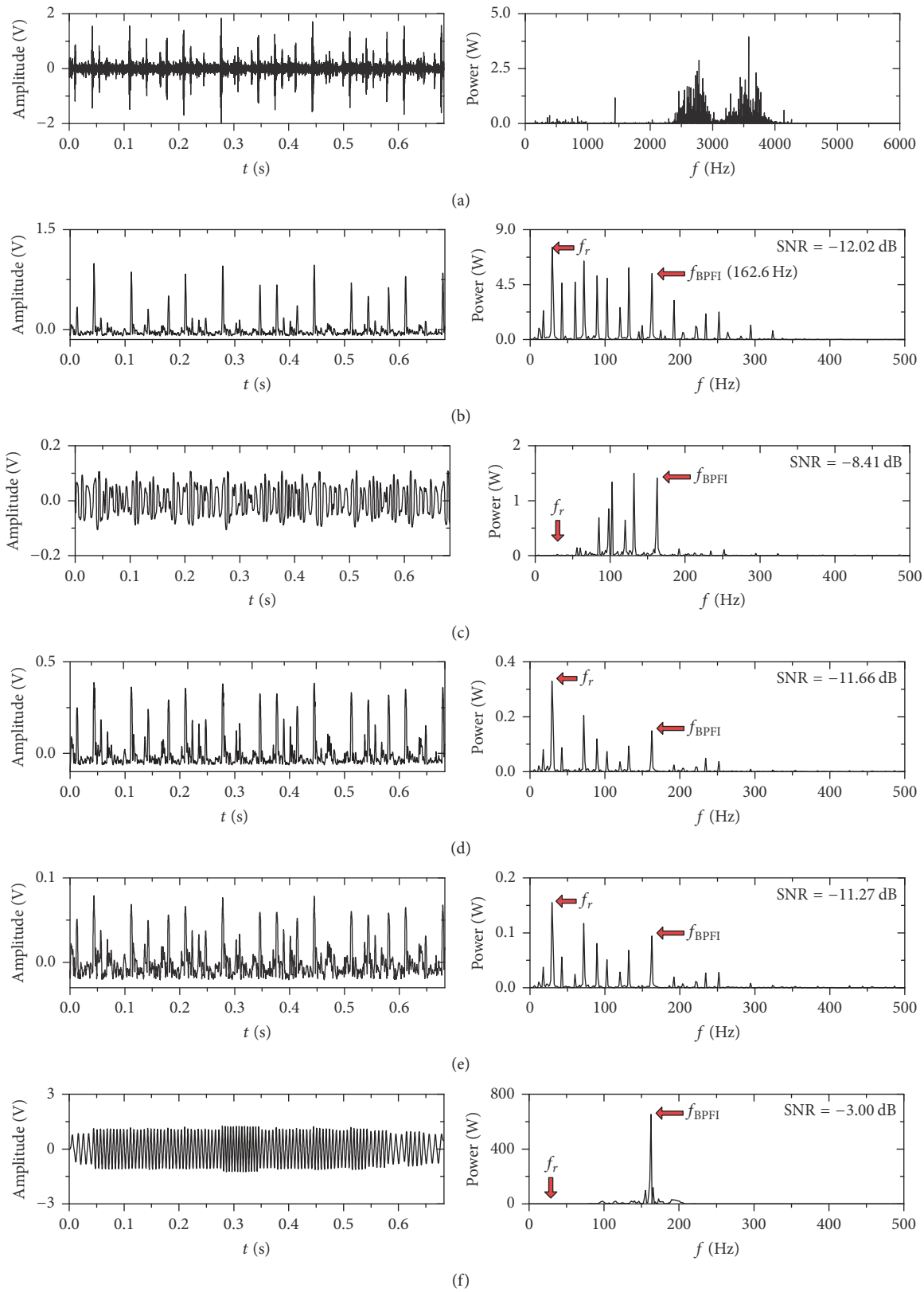

Figure 9: Analysis results for the bearing signal with a defective inner race: (a) original signal; (b) envelope signal with a filtering band at 2500–3000 Hz; (c) optimal MSTSR output signal (optimal parameters: $a = 1e-6$, $b = 8827$, $h = 0.008$, and $K = 6$); (d) optimal WSSR output signal (optimal parameters: $R_1 = 0.3$, $V_0 = 16$, $c = 0.03$, and $h = 0.09$); (e) optimal WSGSR output signal (optimal parameters: $R_1 = 1$, $R_2 = 1$, $V_0 = 18$, $V_1 = 0.8$, $c = 0.4$, and $h = 0.2$); and (f) optimal SVVR output signal (optimal parameters: $a = 1.2$, $b = 5$, $\gamma = 0.008$, $h = 0.05$, $B = 0.06$, and $\Omega = 36505$ rad/s).

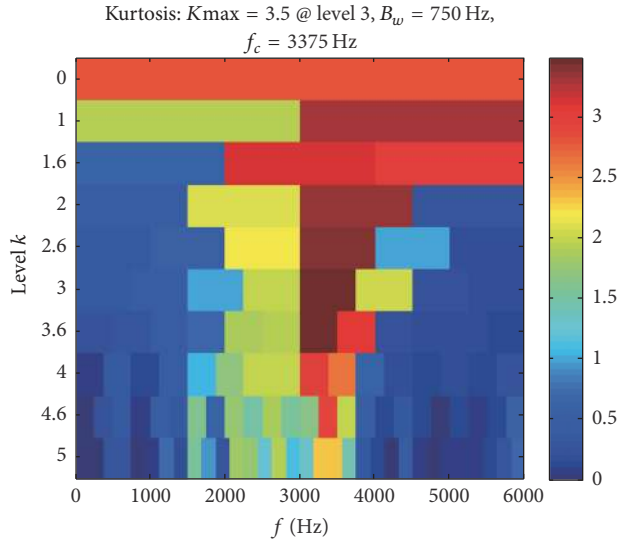

FIGURE 10: Processed results using fast kurtogram for detecting an outer race fault. Central frequency f_c = 3375 Hz, bandwidth B_w = 750 Hz, and level k = 3.

spectrum, and the other noise components tended to zero. From the perspective of noise filtering, f_{BPFI} is extracted in the frequency domain, and the noise components around f_{BPFI} are almost eliminated.

5.2. Fault Detection for the Outer Race of the Bearing. The bearing signal of the defective outer race is analyzed in this section. The obtained results are shown in Figure 11. The proposed SVVR method presents a better filtering performance than MSTSR, WSSR, and WSGSR in the time and frequency domains. The periodicity of the fault signal is improved, and f_{BPFO} can be recognized from the power spectrum. Thus, SVVR is better than the other WSD methods in detecting bearing fault signals.

5.3. Fault Detection for the Rolling Element of the Bearing. The processed results for the bearing signal with a defective rolling element are shown in Figure 13. The results show that the proposed method also detects the objective frequency f_{BSF} effectively. The periodicity is enhanced, and f_{BSF} is highlighted in the frequency domain. The signal enhancement mechanism for SVVR is described as follows. Initially, only one harmonic force is involved; therefore, this force cannot help the particle move across the potential well. The particle energy can be enhanced and can move across the potential well with the assistance of the perturbation of a proper high-frequency periodic harmonic force. Thus, the particle can move freely in the bistable potential well benefiting from the stimulation of the high-frequency signal and, finally, the weak signal can be enhanced.

5.4. Quantitative Analysis. Two evaluation indexes are used to evaluate the fault detection capability of SVVR quantitatively. The first evaluation index is SNR, and the analysis results are listed in Table 3. The SNRs of the fault signals processed by SVVR are higher than those of the other methods. Table 3 shows that SVVR has a better fault detection capability compared with the other methods.

TABLE 3: SNRs with various bearing fault types processed by different WSD methods.

Fault types	Envelope signal SNR (dB)	MSTSR output SNR (dB)	WSSR output SNR (dB)	WSGSR output SNR (dB)	SVVR output SNR (dB)
Inner race	−12.02	−8.41	−11.66	−11.27	−3.00
Outer race	−19.81	−9.23	−12.91	−11.23	−4.27
Rolling element	−26.01	−12.80	−13.42	−12.70	−0.41

Another evaluation index Ind proposed by Wang et al. is discussed to evaluate the fault detection capability of SVVR [43]. Ind is defined as shown in

$$\mathrm{Ind} = \frac{\sum_{j=1}^{5} \mathrm{ES}\left[j \times \mathrm{round}\left(f_F/\Delta f\right) + 1\right]}{\left(\sum_{i=1}^{M} \mathrm{ES}\left[i\right]/M\right)}, \tag{25}$$

where ES[·] represents the discrete envelope spectrum, f_F is the fault characteristic frequency, Δf is the frequency resolution of the fast Fourier transform, and M is the time series length of the envelope spectrum. Equation (25) considers the power of f_F and its harmonics. A high Ind indicates that f_F and its harmonics are highlighted in the envelope spectrum, demonstrating the capability to detect bearing faults [43]. The computed Inds with various fault types of the bearing are listed in Table 4. The Ind calculated using SVVR is higher than those of the other WSD methods. Thus, SVVR can detect defective bearing signals more effectively.

5.5. Discussion. Some discussions are listed as follows:

(1) This paper used the traversal algorithm to search for the optimal parameters, but the convergence rate

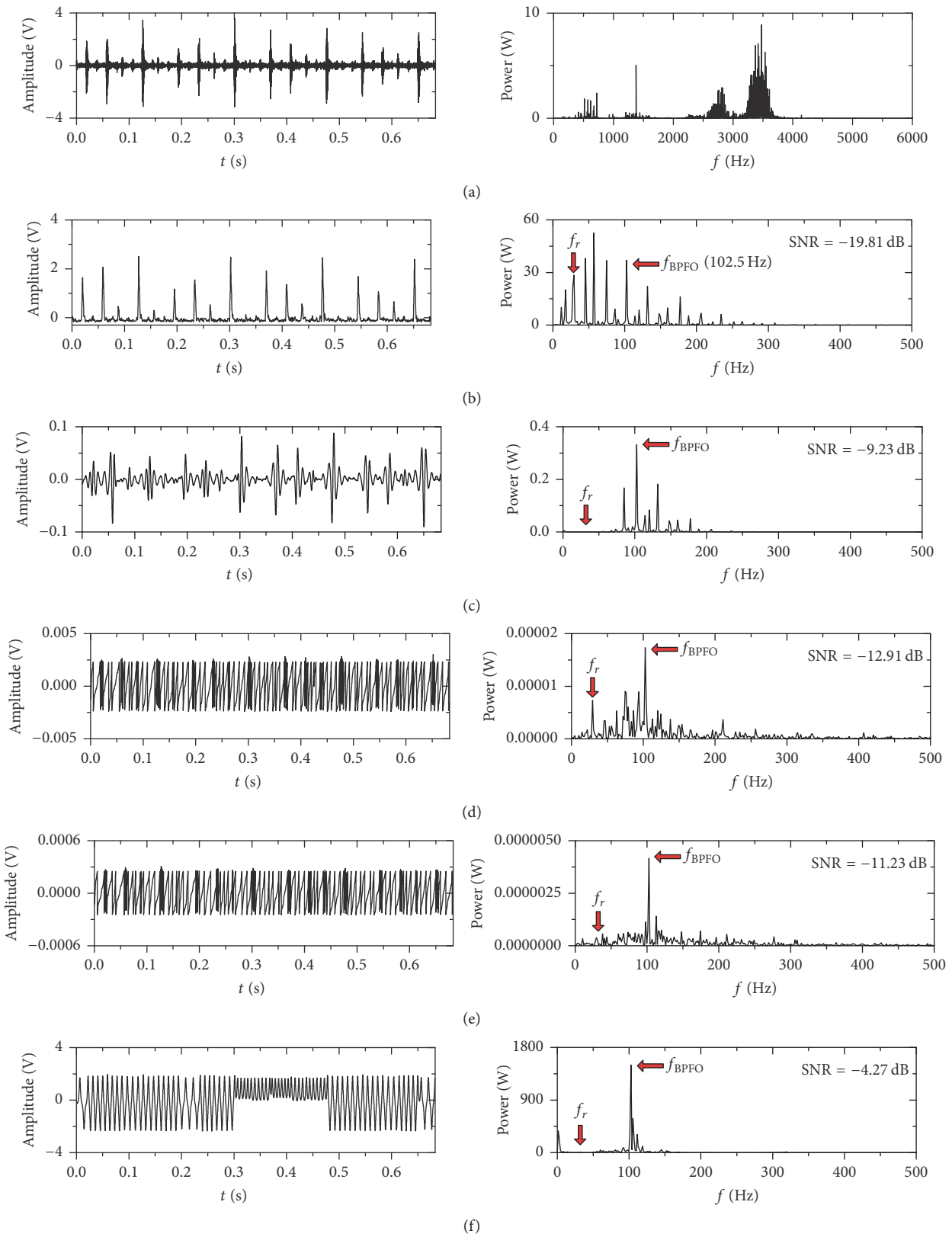

Figure 11: Analysis results for the bearing signal with a defective outer race: (a) original signal; (b) envelope signal with a filtering band at 3000–3750 Hz; (c) optimal MSTSR output signal (optimal parameters: $a = 0.4$, $b = 1$, $h = 2e-4$, and $K = 6$); (d) optimal WSSR output signal (optimal parameters: $R_1 = 0.08$, $V_0 = 36$, $c = 0.6$, and $h = 1e-4$); (e) optimal WSGSR output signal (optimal parameters: $R_1 = 0.05$, $R_2 = 2.1$, $V_0 = 25$, $V_1 = 0.5$, $c = 0.4$, and $h = 4e-5$); and (f) optimal SVVR output signal (optimal parameters: $a = 7.2$, $b = 3.8$, $\gamma = 6e-6$, $h = 0.03$, $B = 4e-5$, and $\Omega = 16736$ rad/s).

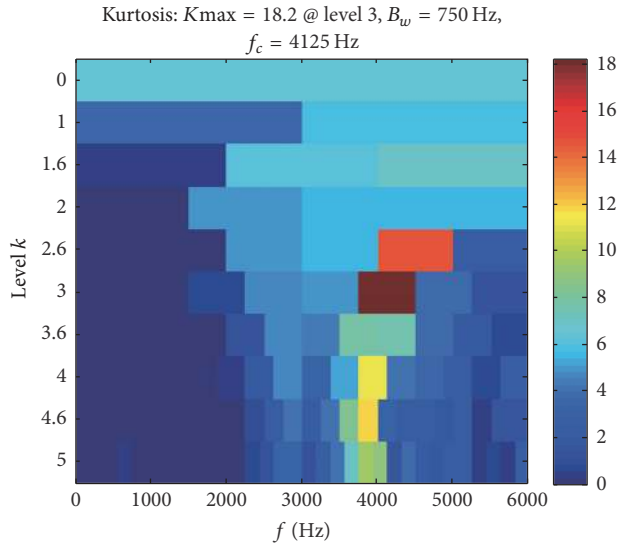

FIGURE 12: Processed results using fast kurtogram for detecting a rolling element fault. Central frequency f_c = 4125 Hz, bandwidth B_w = 750 Hz, and level k = 3.

TABLE 4: Ind's with various bearing fault types processed by different WSD methods.

Fault types	Envelope signal Ind	MSTSR output Ind	WSSR output Ind	WSGSR output Ind	SVVR output Ind
Inner race	248.6	519.2	276.9	133.3	1369.6
Outer race	359.4	1000	386.2	352.1	1120.9
Rolling element	89.4	205	106.9	186.9	649.4

of the traversal algorithm is so slow that it needs a long calculation time. In future works, intelligence algorithms such as genetic algorithms [34], ant colony algorithms [44], and artificial fish swarm algorithms [45] should be used to improve the algorithm efficiency.

(2) The fault type of the bearing may not be related to the resonance frequency band of the band-pass filter. We can calculate the different fault characteristic frequencies of the fault bearings in accordance with the theoretical equations. If the fault type of the bearing is unidentified in advance, the fast kurtogram method can still be used to determine the bandwidth and central frequency of the band-pass filter automatically and intelligently.

(3) Since this study concentrates on VR model and on the filtering effect of VR, the classical evaluation index, SNR, is applied to evaluate the fault detection capability of the proposed SVVR method. However, SNR requires the prior knowledge of the interested signal and this information may not be available in practice. To address this issue, many adaptive methods have been proposed to adaptively enhance weak signals without prior knowledge related to the driving frequency by considering other indexes. For instance, Wang et al. proposed an adaptive index named weighted power spectrum kurtosis for detecting the fault characteristic frequency of the rolling element bearing [45]. Zhou et al. proposed a synthetic index method for extracting the fault characteristic frequency of the rolling element bearing adaptively [46]. In this regard, to make this method more practical, some adaptive indexes could be introduced in the proposed SVVR method, and adaptive VR will be a further study in the future.

(4) Different dynamical systems may affect the output response of VR. In this study, the classical bistable potential is used in VR model to enhance weak signals. Other potentials, such as monostable potential, tristable potential, and exponential potential, might be introduced in weak signal enhancement and bearing fault diagnosis. This point deserves to be a further study in the future.

6. Conclusion

The WSD method SVVR is proposed to extract the fault characteristic frequency, which is overwhelmed by heavy background noise. Weak signals can be enhanced by optimizing the parameters. Finally, the periodicity of the weak input signal can be recognized in the time domain. The proposed method has following advantages: (1) the output signal presents good periodicity; (2) antinoise performance analysis shows that the SNR is increased; and (3) frequency response analysis indicates that SVVR serves as a band-pass filter because it can filter low- and high-frequency noise components. Consequently, SVVR can effectively suppress heavy background noise. Simulation and engineering signals are used to verify the practicability of SVVR. SVVR can improve the fault detection capability, thereby benefiting for bearing

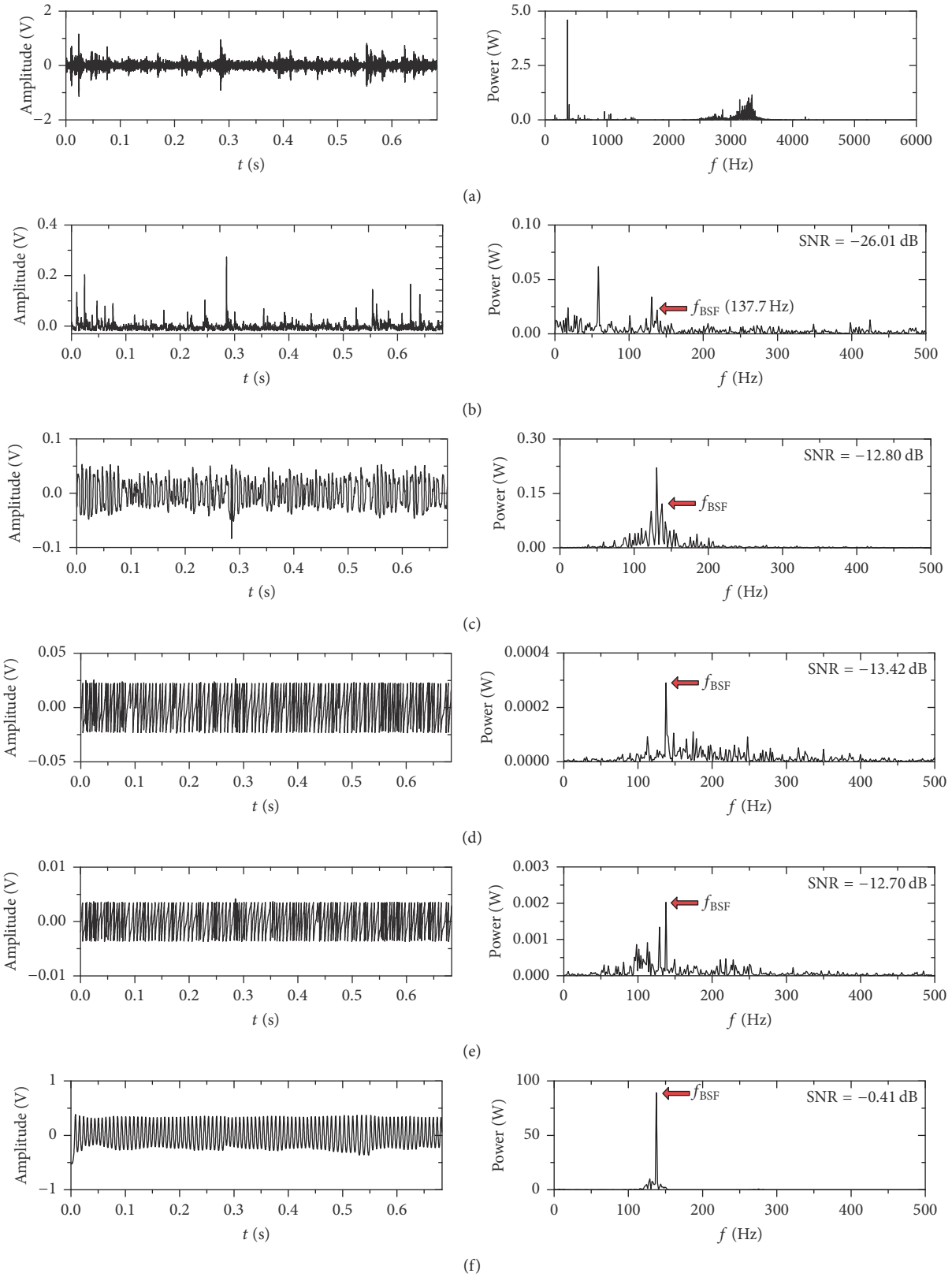

FIGURE 13: Analysis results for the bearing signal with a defective rolling element: (a) original signal; (b) envelope signal with a filtering band at 3750–4500 Hz; (c) optimal MSTSR output signal (optimal parameters: $a = 2e - 14$, $b = 8800$, $h = 0.034$, and $K = 6$); (d) optimal WSSR output signal (optimal parameters: $R_1 = 0.002$, $V_0 = 10$, $c = 1.5$, and $h = 0.004$); (e) optimal WSGSR output signal (optimal parameters: $R_1 = 1e - 3$, $R_2 = 3.7$, $V_0 = 12$, $V_1 = 0.5$, $c = 1.3$, and $h = 0.007$); and (f) optimal SVVR output signal (optimal parameters: $a = 1.9$, $b = 4.6$, $\gamma = 8e - 5$, $h = 0.044$, $B = 0.006$, and $\Omega = 12354$ rad/s).

fault recognition. The proposed method shows application prospects in rotary machine fault detection and other fields concerned with weak periodic signal enhancement.

Conflicts of Interest

The authors declare that they have no conflicts of interest.

Acknowledgments

This work is supported in part by the National Natural Science Foundation of China (nos. 51675001, 51605002, and 51505001) and the Natural Science Foundation of Anhui Province (nos. 1608085QE110 and 1508085SQE212). The authors are grateful to the CWRU for providing free-bearing data download.

References

[1] F. Liu, B. He, Y. Liu, S. Lu, Y. Zhao, and J. Zhao, "Phase space similarity as a signature for rolling bearing fault diagnosis and remaining useful life estimation," *Shock and Vibration*, vol. 2016, Article ID 5341970, 12 pages, 2016.

[2] Y. Liu, B. He, F. Liu, S. Lu, and Y. Zhao, "Feature fusion using kernel joint approximate diagonalization of eigen-matrices for rolling bearing fault identification," *Journal of Sound & Vibration*, vol. 385, pp. 389–401, 2016.

[3] L. Cui, Y. Zhang, F. Zhang, J. Zhang, and S. Lee, "Vibration response mechanism of faulty outer race rolling element bearings for quantitative analysis," *Journal of Sound and Vibration*, vol. 364, pp. 67–76, 2016.

[4] J. Wang, Y. Peng, and W. Qiao, "Current-aided order tracking of vibration signals for bearing fault diagnosis of direct-drive wind turbines," *IEEE Transactions on Industrial Electronics*, vol. 63, no. 10, pp. 6336–6346, 2016.

[5] X. Xiang and B. Shi, "Weak signal detection based on the information fusion and chaotic oscillator," *Chaos*, vol. 20, no. 1, pp. 135–138, 2010.

[6] M. Zhao, J. Lin, Y. Miao, and X. Xu, "Detection and recovery of fault impulses via improved harmonic product spectrum and its application in defect size estimation of train bearings," *Measurement: Journal of the International Measurement Confederation*, vol. 91, pp. 421–439, 2016.

[7] X. Zhang, N. Hu, G. Qin, Z. Cheng, and H. Zhong, "A bearing fault detection method based on compressive measurements of vibration signal," *Journal of Vibroengineering*, vol. 16, no. 3, pp. 1200–1211, 2014.

[8] S. Lu, Q. He, and F. Kong, "Effects of underdamped step-varying second-order stochastic resonance for weak signal detection," *Digital Signal Processing*, vol. 36, pp. 93–103, 2015.

[9] B. Jiang, J. Xiang, and Y. Wang, "Rolling bearing fault diagnosis approach using probabilistic principal component analysis denoising and cyclic bispectrum," *Journal of Vibration and Control*, vol. 22, no. 10, pp. 2420–2433, 2014.

[10] M. Žvokelj, S. Zupan, and I. Prebil, "Non-linear multivariate and multiscale monitoring and signal denoising strategy using Kernel Principal Component Analysis combined with Ensemble Empirical Mode Decomposition method," *Mechanical Systems and Signal Processing*, vol. 25, no. 7, pp. 2631–2653, 2011.

[11] A. Mert and A. Akan, "Detrended fluctuation thresholding for empirical mode decomposition based denoising," *Digital Signal Processing: A Review Journal*, vol. 32, pp. 48–56, 2014.

[12] W. Li, F. Gu, A. D. Ball, A. Y. T. Leung, and C. E. Phipps, "A study of the noise from diesel engines using the independent component analysis," *Mechanical Systems and Signal Processing*, vol. 15, no. 6, pp. 1165–1184, 2001.

[13] Q. He and J. Wang, "Effects of multiscale noise tuning on stochastic resonance for weak signal detection," *Digital Signal Processing*, vol. 22, no. 4, pp. 614–621, 2012.

[14] P. Shi, C. Su, and D. Han, "Fault diagnosis of rotating machinery based on adaptive stochastic resonance and AMD-EEMD," *Shock and Vibration*, vol. 2016, Article ID 9278581, 11 pages, 2016.

[15] J. Dang, R. Jia, X. Luo, H. Wu, and D. Chen, "Partly duffing oscillator stochastic resonance method and its application on mechanical fault diagnosis," *Shock and Vibration*, vol. 2016, Article ID 3109385, 14 pages, 2016.

[16] J. Li and J. Zhang, "Adaptive multiscale noise control enhanced stochastic resonance method based on modified EEMD with its application in bearing fault diagnosis," *Shock and Vibration*, vol. 2016, Article ID 1485412, 2016.

[17] M. Bordet and S. Morfu, "Experimental and numerical enhancement of vibrational resonance in neural circuit," *Electronics Letters*, vol. 48, no. 15, pp. 903–905, 2012.

[18] R. Benzi, A. Sutera, and A. Vulpiani, "The mechanism of stochastic resonance," *Journal of Physics. A. Mathematical and General*, vol. 14, no. 11, pp. L453–L457, 1981.

[19] D. Rousseau and F. Chapeau-Blondeau, "Stochastic resonance and improvement by noise in optimal detection strategies," *Digital Signal Processing*, vol. 15, no. 1, pp. 19–32, 2005.

[20] Y. Xu, J. Wu, H.-Q. Zhang, and S.-J. Ma, "Stochastic resonance phenomenon in a underdamped bistable system driven by weak asymmetric dichotomous noise," *Nonlinear Dynamics*, vol. 70, no. 1, pp. 531–539, 2012.

[21] F. Chapeau-Blondeau, "Stochastic resonance and optimal detection of pulse trains by threshold devices," *Digital Signal Processing: A Review Journal*, vol. 9, no. 3, pp. 162–177, 1999.

[22] B. McNamara and K. Wiesenfeld, "Theory of stochastic resonance," *Physical Review A*, vol. 39, no. 9, pp. 4854–4869, 1989.

[23] P. S. Landa and P. V. McClintock, "Vibrational resonance," *Journal of Physics. A. Mathematical and General*, vol. 33, no. 45, pp. L433–L438, 2000.

[24] J. H. Yang and X. B. Liu, "Controlling vibrational resonance in a multistable system by time delay," *Chaos*, vol. 20, no. 3, pp. 447–457, 2010.

[25] J. H. Yang and H. Zhu, "Vibrational resonance in Duffing systems with fractional-order damping," *Chaos*, vol. 22, no. 1, pp. 149–159, 2012.

[26] A. Daza, A. Wagemakers, and M. A. Sanjuán, "Strong sensitivity of the vibrational resonance induced by fractal structures," *International Journal of Bifurcation and Chaos in Applied Sciences and Engineering*, vol. 23, no. 7, Article ID 1350129, 8 pages, 2013.

[27] I. I. Blekhman and P. S. Landa, "Conjugate resonances and bifurcations in nonlinear systems under biharmonical excitation," *International Journal of Non-Linear Mechanics*, vol. 39, no. 3, pp. 421–426, 2004.

[28] G. P. Harmer and D. Abbott, "Simulation of circuits demonstrating stochastic resonance," *Microelectronics Journal*, vol. 31, no. 7, pp. 553–559, 2000.

[29] F. Duan, F. Chapeau-Blondeau, and D. Abbott, "Enhancing array stochastic resonance in ensembles of excitable systems," *Journal of Statistical Mechanics: Theory and Experiment*, vol. 32, pp. 55–62, 2009.

[30] F. Chapeau-Blondeau and X. Godivier, "Theory of stochastic resonance in signal transmission by static nonlinear systems," *Physical Review E*, vol. 55, no. 2, pp. 1478–1495, 1997.

[31] J. Li, Y. Zhang, and P. Xie, "A new adaptive cascaded stochastic resonance method for impact features extraction in gear fault diagnosis," *Measurement: Journal of the International Measurement Confederation*, vol. 91, pp. 499–508, 2016.

[32] S. Zhang, S. Lu, Q. He, and F. Kong, "Time-varying singular value decomposition for periodic transient identification in bearing fault diagnosis," *Journal of Sound and Vibration*, vol. 379, pp. 213–231, 2016.

[33] J. Altmann and J. Mathew, "Multiple band-pass autoregressive demodulation for rolling-element bearing fault diagnosis," *Mechanical Systems and Signal Processing*, vol. 15, no. 5, pp. 963–977, 2001.

[34] Q. B. He, J. Wang, F. Hu, and F. Kong, "Wayside acoustic diagnosis of defective train bearings based on signal resampling and information enhancement," *Journal of Sound and Vibration*, vol. 332, no. 21, pp. 5635–5649, 2013.

[35] S. Lu, Q. He, and F. Kong, "Stochastic resonance with Woods–Saxon potential for rolling element bearing fault diagnosis," *Mechanical Systems and Signal Processing*, vol. 45, no. 2, pp. 488–503, 2014.

[36] H. Zhang, Q. He, S. Lu, and F. Kong, "Stochastic resonance with a joint Woods-Saxon and Gaussian potential for bearing fault diagnosis," *Mathematical Problems in Engineering*, vol. 2014, Article ID 315901, 17 pages, 2014.

[37] W. A. Smith and R. B. Randall, "Rolling element bearing diagnostics using the Case Western Reserve University data: a benchmark study," *Mechanical Systems and Signal Processing*, vol. 64-65, pp. 100–131, 2015.

[38] R. B. Randall and J. Antoni, "Rolling element bearing diagnostics—a tutorial," *Mechanical Systems and Signal Processing*, vol. 25, no. 2, pp. 485–520, 2011.

[39] K. Belalouache, D. Benazzouz, and C. Rahmoune, "1390. A new method based on fast Kurtogram for the identification of pitting fault versus crack fault in gearbox systems," *Journal of Vibroengineering*, vol. 16, no. 6, pp. 2974–2982, 2014.

[40] D. Wang, P. W. Tse, and K. L. Tsui, "An enhanced Kurtogram method for fault diagnosis of rolling element bearings," *Mechanical Systems and Signal Processing*, vol. 35, no. 1-2, pp. 176–199, 2013.

[41] P. W. Tse and D. Wang, "The design of a new sparsogram for fast bearing fault diagnosis: part 1 of the two related manuscripts that have a joint title as 'Two automatic vibration-based fault diagnostic methods using the novel sparsity measurement—parts 1 and 2'," *Mechanical Systems and Signal Processing*, vol. 40, no. 2, pp. 499–519, 2013.

[42] D. Wang and K. Tsui, "Dynamic Bayesian wavelet transform: New methodology for extraction of repetitive transients," *Mechanical Systems and Signal Processing*, vol. 88, pp. 137–144, 2017.

[43] D. Wang, Q. Miao, X. Fan, and H.-Z. Huang, "Rolling element bearing fault detection using an improved combination of Hilbert and wavelet transforms," *Journal of Mechanical Science and Technology*, vol. 23, no. 12, pp. 3292–3301, 2010.

[44] X. Li, A. Zheng, X. Zhang, C. Li, and L. Zhang, "Rolling element bearing fault detection using support vector machine with improved ant colony optimization," *Measurement*, vol. 46, no. 8, pp. 2726–2734, 2013.

[45] J. Wang, Q. B. He, and F. R. Kong, "Adaptive multiscale noise tuning stochastic resonance for health diagnosis of rolling element bearings," *IEEE Transactions on Instrumentation and Measurement*, vol. 64, no. 2, pp. 564–577, 2015.

[46] P. Zhou, S. Lu, F. Liu, Y. Liu, G. Li, and J. Zhao, "Novel synthetic index-based adaptive stochastic resonance method and its application in bearing fault diagnosis," *Journal of Sound and Vibration*, vol. 391, pp. 194–210, 2017.